Friction

Research Article

Investigation of the influence of substrate hardness on the tribological performance of graphene oxide solid lubricant coatings

Yuzhen Liu[1,2,3], Hui Chen[3,✉], Wenli Wang[1,2,3], Kai Le[1,2], Guoqing Wang[4], Yong Luo[3], Xiaoming Gao[1], Xu Zhao[1], Xingnan Liu[1,2,3], Shusheng Xu[1,2,✉], Dae-Eun Kim[4], Weimin Liu[1]

Cite this article: Liu YZ, Chen H, Wang WL, et al. *Friction* 2025, **13**(10): 9441085. https://doi.org/10.26599/FRICT.2025.9441085

ABSTRACT: This study explores the impact of substrate hardness on the tribological properties of graphene oxide (GO) solid lubricant coatings on NiP alloy layers coated Q235 steel. Through adjustment of electroless plating parameters, NiP alloy layers with varying hardness levels were produced to investigate their effects on the wear resistance and friction performance of GO coatings. The methodology included substrate preparation, electroless NiP alloy plating, electrophoresis deposition of GO, and detailed analysis of the structural, mechanical, and tribological characteristics of the coatings. These findings underscore the crucial role of substrate hardness in the tribological efficiency of GO coatings. A specific hardness level emerged as optimal, significantly enhancing the distribution and effectiveness of the GO tribofilm. This uniform and continuous tribofilm led to notable improvements in the wear resistance and a reduction in friction coefficients. Moreover, this optimal hardness ensured continuous lubrication and superior load-bearing capabilities, substantially prolonging the lifespan of the coatings. Substrates with hardness levels that were either too high or too low were observed to hinder the maintenance of a consistent tribofilm, thereby negatively impacting the tribological performance of the coating. This research highlights the importance of achieving an optimal substrate hardness to enhance the tribological performance of solid lubricant coatings. By optimizing the balance between the substrate hardness and integrity of the tribofilm, this study paves the way for developing more efficient, durable, and environmentally sustainable mechanical components, offering new insights into tribological science and materials engineering.

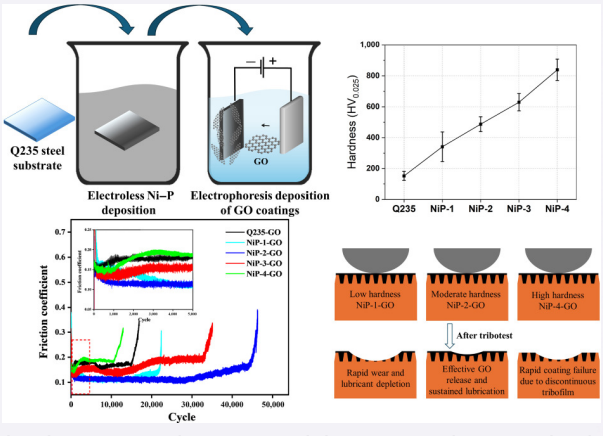

KEYWORDS: electroless-plated NiP coating; graphene oxide (GO) coating; hardness; tribology

1 Introduction

Tribology, the science of understanding friction, wear, and lubrication, is pivotal in determining the functionality and longevity of mechanical systems. Friction and wear, especially in the relative motion of mechanical parts, are significant contributors to energy and material losses [1, 2]. It is estimated that over 50% of global energy consumption is linked to various types of power machinery, yet only approximately 30% of this energy is effectively utilized. Moreover, wear and tear contribute to approximately 60% of equipment damage and failure [3, 4]. There is an urgent need for improved lubrication solutions in industries such as aviation, space science and technology, and electronic information due to increasing demands. Lubrication and surface strengthening technologies have become vital strategies to address these challenges [5–7].

Solid lubricants have emerged as essential tools for reducing friction and wear at interfaces, with graphene oxide (GO) standing out because of its remarkable properties, including exceptional mechanical strength, high thermal conductivity, and low friction coefficients [8–10]. However, the tribological performance of GO coatings is influenced by factors such as working conditions, environmental humidity, substrate roughness, and mechanical properties [11, 12]. Berman et al. [13] reported that the durability

[1] State Key Laboratory of Solid Lubrication, Lanzhou Institute of Chemical Physics, Chinese Academy of Sciences, Lanzhou 730000, China. [2] Shandong Laboratory of Advanced Materials and Green Manufacturing at Yantai, Yantai 264000, China. [3] School of Materials Science and Engineering, China University of Mining and Technology, Xuzhou 221116, China. [4] Department of Mechanical Engineering, Yonsei University, Seoul 03722, Republic of Korea.

✉ Corresponding authors. E-mail: S. Xu,ssxu@licp.cas.cn; H. Chen, chenhui03990758@163.com

Received: March 4, 2024; Revised: January 11, 2025; Accepted: February 27, 2025

of graphene-based lubricating coatings was related to the contact level at friction interfaces. For example, under a 5 N normal load, the graphene coating quickly wore away, leading to increased friction and wear. However, at a 1 N load, both the friction and wear remained low, with the friction coefficient being four times less than that at a 5 N load. Reinert et al. [14] observed that the lubricating effectiveness of carbon nanoparticles was affected by surface roughness. If the roughness exceeded the diameters of the nanoparticles, they were trapped in substrate surface grooves, reducing their lubricating ability [15]. Larger, high aspect ratio carbon nanoparticles engaged more directly in the sliding interface and were less affected by surface roughness. Bhowmick et al. [16] reported that the tribological properties of graphene on Ti6Al4V alloy surfaces varied with humidity. A high friction coefficient of 0.52 in dry N_2 atmosphere decreased to 0.11 at 10% relative humidity (RH), with further reductions as the humidity increased due to the passivating effect of H and OH groups. Morstein and Dienwiebel [17] noted a 3.6-fold increase in the friction coefficient when the graphene film thickness increased from 0.2 to 17 μm, suggesting that thicker films extend the friction life and reduce the wear. Yao et al. [18] highlighted that substrate stiffness influenced the tribological characteristics of graphene coatings. Simulation results suggest that a stiffer substrate minimizes graphene deformation, effectively distributing load and enhancing load-bearing capacity, thereby improving the wear resistance. Therefore, the performance of solid lubricants at interfaces is multifaceted and influenced by various factors, including substrate hardness, which warrants further investigation. Low-strength metals and alloys are valued for their plasticity and toughness but are often limited by their low hardness, high friction coefficients, and chemical reactivity, making them unsuitable for high-stress applications [19–21]. Surface treatments, such as hard coatings, have been employed to improve hardness and wear resistance, enabling their use in demanding friction environments [20, 22]. Despite these advancements, the precise mechanisms through which the substrate hardness affects the tribological behavior of GO coatings, as well as the optimal hardness levels for maximum performance, remain underexplored.–

This study combines the development of NiP alloy layers with GO solid lubricants, addressing a critical gap in the current understanding of substrate–coating interactions. Through electroless plating, NiP alloy layers with tunable hardnesses were fabricated on Q235 steel, enabling a systematic investigation into the influence of substrate hardness on the tribological performance of GO coatings. By increasing the hardness and load-bearing capacity of low-strength materials and analyzing the tribological behavior of GO solid lubricants, this work provides valuable insights into the wear resistance, friction reduction, and failure mechanisms of these materials. The findings reveal that substrate hardness significantly influences the tribological performance of GO solid lubricant coatings, with a moderate hardness level providing optimal wear resistance, consistent lubrication, and extended coating lifetime. Excessively high or low hardness levels compromise the integrity and functionality of the tribofilm, highlighting the importance of achieving a balanced substrate hardness for superior tribological properties.

2 Experimental procedures

2.1 Substrate treatments and electroless NiP plating coating deposition

Q235 steel with a size of 20 mm × 20 mm × 2 mm was selected as the substrate material for this study. Prior to the deposition of the electroless NiP coating, the steel samples underwent a preparatory process. Initially, they were polished with 100-grade sandpaper. The samples were subsequently cleaned sequentially with petroleum ether and anhydrous ethanol for 10 min each to ensure the removal of any surface contaminants. The next step involved degreasing the samples in an alkaline solution, as specified in Table 1, at a controlled temperature of 55 °C for 10 min. This process was crucial for eliminating any residual grease or oil. Subsequently, the samples were thoroughly rinsed with distilled water to remove alkaline solution residues. The surface activation step involved immersing the samples in 10 wt% HCl solution for 2 min. This step aimed to activate the surface and remove potential oxidation layers, preparing the steel for effective coating adhesion. A second rinse with distilled water was performed to ensure complete removal of the acidic solution. Finally, the prepared samples were placed in an electroless plating bath. The specific conditions employed for the electroless plating process, which resulted in the formation of four distinct NiP samples labeled NiP-1, NiP-2, NiP-3, and NiP-4 (detailed in Table 2).

2.2 Electrophoretic deposition of GO coatings

The GO coating was deposited as a separate layer on top of the NiP substrate, with the NiP layer providing mechanical strength and corrosion resistance, while the GO layer functions as the primary tribological interface. This two-layer structure enables the evaluation of the tribological performance of GO as a solid lubricant, which is influenced by the mechanical properties of the underlying NiP layer. GO coatings were uniformly deposited on NiP alloy coatings using electrophoretic deposition (EPD) [23–25]. The deposition solution was composed of 1.5 g/L GO nanopowder dispersed in distilled water. Initially, this mixture was stirred for 20 min, followed by ultrasonic dispersion for 4 min to ensure uniform dispersion of the GO nanopowder. During the deposition process, a consistent 10-V direct current (DC) voltage was applied across the electrodes to make the Q235 steel. The selection of 10 V for EPD was based on the optimization experiments, where lower voltages led to insufficient deposition

Table 1 Composition of alkaline solution for degreasing

Chemical composition	Na_2CO_3	NaOH	$CHSO_4Na$
Content (wt%)	2.5	2.5	0.2

Table 2 Chemical compositions and process conditions of electroless-plated NiP samples

Chemical composition and process condition	NiP-1	NiP-2	NiP-3	NiP-4
$NiSO_4$ (g/L)	30	30	36	36
NaH_2PO_2 (g/L)	25	25	28	28
$C_2H_3NaO_2$ (g/L)	15	15	34	34
$C_6H_5Na_3O_7{\cdot}2H_2O$ (g/L)	20	20	0	0
$C_3H_6O_3$ (g/L)	10	10	12.4	12.4
CH_4N_2S (g/L)	0	0.76	1.52	1.52
KI (g/L)	0	0	4	4
$CuSO_4$ (g/L)	4	0	0	0
pH	4.6	4.6	5.2	5.2
Time (min)	45	45	45	45
Temperature (°C)	88±2	88±2	88±2	88±2
Heat treatment	—	—	—	400 °C for 60 min

and higher voltages caused particle aggregation and uneven coatings. At 10 V, the optimal deposition efficiency and uniformity were achieved. Similarly, the temperature of 88 °C for NiP deposition was chosen based on both the literature and experimental results, as it fell within the optimal range (80–90 °C) for facilitating co-deposition while ensuring coating density and mechanical stability [26]. This application was sustained for 10 min, facilitating the deposition of the GO coating onto the NiP alloy coatings within the prepared solution, as illustrated in Fig. 1. The deposition time for the EPD process was determined through a series of optimization experiments. Deposition time shorter than 1–2 min resulted in inadequate coverage and nonuniform coatings, while durations exceeding 15 min produced overly thick GO layers, leading to particle aggregation and increased surface roughness. 10-min deposition time was identified as the optimal duration, ensuring a uniform, high-quality, and consistent GO coating. After deposition, the samples were dried in a vacuum oven at 50 °C for 2 h. This step was critical for ensuring proper adhesion and stability of the GO coating on the NiP alloy. The resulting GO-coated NiP alloys were designated as NiP-1-GO, NiP-2-GO, NiP-3-GO, and NiP-4-GO.

2.3 Structure characterization

The morphology and chemical composition of the coatings were characterized using a scanning electron microscope (SEM; FEI Quanta FEG 250) equipped with an energy dispersive spectrometer (EDS; Oxford XMax). The microstructures of the samples were determined using an X-ray diffractometer (XRD; D/MAX-RB, Rigaku) using Cu-Kα radiation at a scanning speed of 1 (°)/min and a step size of 0.02°. The surface morphology and roughness were assessed using a three-dimensional (3D) laser scanning confocal microscope (LSCM; Keyence VKX200K). In addition, the microstructure of the wear tracks was examined using a Raman microscope (Thermo Fisher, DXR2), employing an argon-ion laser for excitation at a wavelength of 532 nm and a power setting of 0.5 mW.

2.4 Mechanical and tribological property measurements

The mechanical properties of the electroless NiP coating, specifically the elastic modulus and nanohardness, were measured via a nanoindenter system (Hysitron TriboIndenter), which applied a load of 75 mN fora duration of 10 s. Furthermore, the cross-sectional hardness of the electroless NiP coating was evaluated with a Vickers microhardness tester (FM-700), which applied a load of 0.25 N for 15 s. To ensure repeatability and reliability of the experimental findings, each sample was subjected to five tests, and the average values were calculated. Tribotests were conducted via a ball-on-disk tribometer. In these tests, a 440C steel ball, characterized by a hardness of 650 $HV_{0.025}$ and a diameter of 8 mm, was employed as the counterface material. The experiments were carried out in a controlled environment with the humidity maintained at 20% RH. During the tribotests, a normal load of 5 N was consistently applied. The tribometer was set to a turning radius of 4 mm and a sliding velocity of 0.126 m/s. This ensured uniform test conditions across all the samples. To enhance the reliability of the results, each sample was subjected to testing three times. Repetition of tests under these controlled conditions is critical for ensuring the consistency and reproducibility of the data [27]. The wear tracks were further analyzed by using an optical microscope (U3CMOS, Hangzhou ToupTek Photonics Co., Ltd.), Raman microscope, SEM, EDS, and transmission electron microscope (TEM; FEI Tecnai G2 F30). These analyses can provide comprehensive insights into the wear behavior of GO-coated NiP coatings.

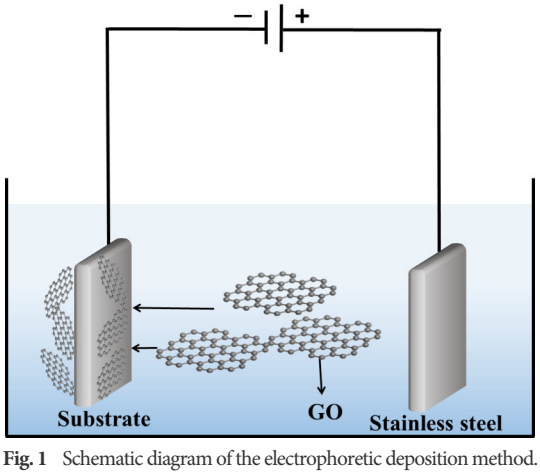

Fig. 1 Schematic diagram of the electrophoretic deposition method.

3 Results and discussion

3.1 Morphology and component of NiP coatings

The optical microscopy images presented in Figs. 2(a)–2(d) depict the cross-sectional views of the electroless coatings on the NiP-1, NiP-2, NiP-3, and NiP-4 samples, respectively. These images reveal that the coatings applied to the Q235 steel substrates are characterized by their uniform thickness and a clearly defined interface with the substrate material. Specifically, the thickness of the NiP-1 coating is measured at 13.5 μm, the NiP-2 coating at 13.6 μm, and both the NiP-3 and NiP-4 coatings exhibit a thickness of 13.4 μm. The observed uniformity in thickness across these samples can be attributed to the chemical consistency maintained in the plating solution, as well as to the adaptable morphology inherent to the electroless plating process.

Figure 3 presents the XRD patterns for the NiP-1, NiP-2, NiP-3, and NiP-4 samples. As shown in Fig. 3(a), the XRD patterns of the electroless NiP-1 and NiP-2 samples exhibit a diffraction peak at a 2θ angle of 44.5°, which corresponds to the Ni(111) plane (JCPDS00-004-0850) [28, 29]. The diffuse nature of these peaks indicates an amorphous phase structure in both the NiP-1 and NiP-2 samples [30]. Conversely, Fig. 3(b) illustrates a more defined Ni(111) peak for NiP-3 at the same 2θ angle, suggesting a transition towards a crystalline state. In the case of NiP-4, the emergence of distinct diffraction peaks at 2θ angles of 44.5°, 51.8°, and 76.4°, corresponding to the Ni(111), (200), and (220) planes, respectively, is indicative of a more crystalline structure [31]. This inference is further supported by the increased intensity and narrowing of the half width of the Ni diffraction

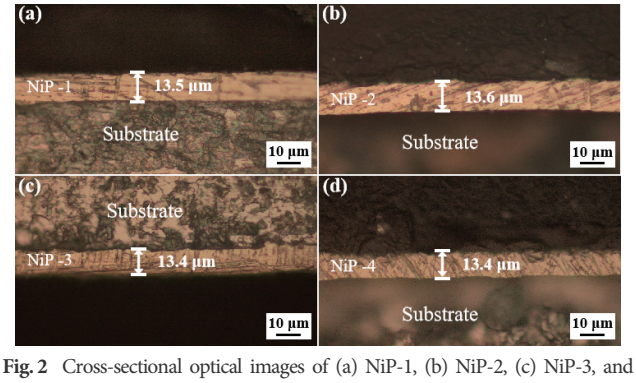

Fig. 2 Cross-sectional optical images of (a) NiP-1, (b) NiP-2, (c) NiP-3, and (d) NiP-4 samples.

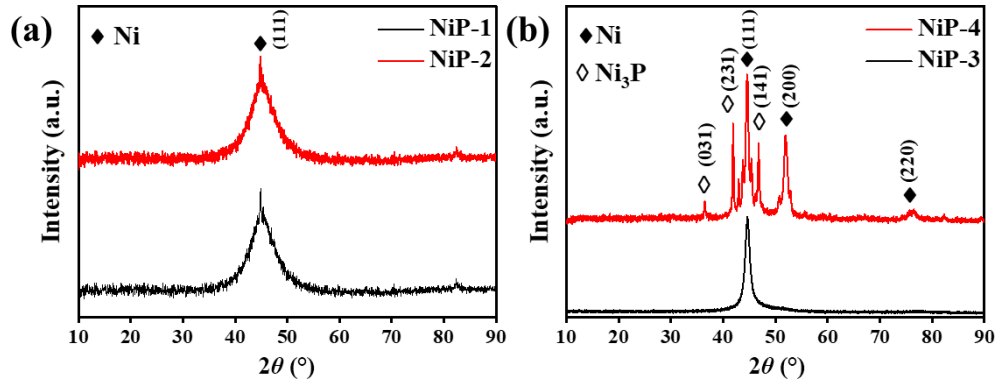

Fig. 3 XRD patterns of (a) NiP-1 and NiP-2, and (b) NiP-3 and NiP-4 samples.

peaks, implying larger grain sizes in the NiP coating. Moreover, the sharp diffraction peaks observed at 2θ angles of 36.4°, 41.7°, and 46.6° in NiP-4, corresponding to (031), (231), and (141) planes of Ni_3P (JCPDS00-034-0501), respectively, confirm the transformation of the electroless coating from an amorphous to a crystalline structure following heat treatment [32]. The NiP coatings with different deposition and annealing processes possess distinct phase structures that can determine the mechanical properties.

Figures 4(a)–4(e) illustrate the 3D surface profiles of the Q235 steel, NiP-1, NiP-2, NiP-3, and NiP-4 samples, revealing their detailed surface topography. Similarly, Figs. 4(a1)–4e(1) depict the two-dimensional (2D) cross-sectional surface profiles of these samples, offering a comprehensive perspective of the surface structures in cross-sections. As demonstrated in Fig. 5, the surface roughness (R_a) values are measured to be 638.91 nm for Q235 steel, 656.02 nm for NiP-1, 667.63 nm for NiP-2, 659.66 nm for NiP-3, and 678.70 nm for NiP-4, respectively. These measurements reveal that the roughness of the NiP-coated samples is relatively uniform, exhibiting only a slight increase in roughness compared with that of the untreated Q235 steel. This minimal variation in roughness across the samples is attributed to the consistent deposition quality afforded by the electroless plating process. Furthermore, the variance in roughness values among the four NiP-coated samples is within a reasonable error margin, indicating a high level of consistency in the electroless plating process.

3.2 Structure of NiP–GO lubricating coating

The SEM image of the GO powder, presented in Fig. 6(a), shows its characteristic sheet-like structure. The XRD pattern of the NiP-1-GO sample, shown in Fig. 6(b), reveals distinct peaks correlating with the crystalline structure of the components. Notably, a prominent peak at a 2θ angle of 10.06° corresponds to the (002) crystal plane of GO [33]. Additionally, a peak observed at a 2θ angle of 44.50° is aligned with the (111) crystal plane of Ni (JCPDS00-004-0850). These findings indicate the successful deposition of the GO lubricating coating on the surface of the electroless NiP alloy sample. To determine the thickness of the GO coating, a mechanical method was utilized to remove the surface layer of GO. Figures 6(c) and 6(d) show the 3D topography and 2D profile, respectively, of the area from which the GO layer was removed. Based on these analyses, the thickness of the GO coating is estimated to be approximately 2.5 μm. The GO coating, which is inherently soft, functions as a solid lubricant by forming a thin, stable tribofilm on friction surfaces during sliding, effectively reducing friction and wear. While the EPD process was optimized to ensure uniform coating thickness, minor variations have a minimal impact on tribological performance, as the mechanism depends more on the quality and stability of the tribofilm than on the initial coating thickness. Efforts were made to maintain coating uniformity to ensure consistency and minimize localized effects in the experimental results.

3.3 Mechanical performance analysis of NiP coatings

The Vickers hardness of the Q235 steel and the NiP-1, NiP-2, NiP-3, and NiP-4 samples was evaluated via a microhardness tester, which focused on the cross-sectional area of the coatings. During these assessments, a load of 25 g was applied for a duration of 10 s and then released. To improve the accuracy of the results, the hardness of each sample was measured five times, and an average value was subsequently calculated. Following the measurements, an optical microscope was employed to confirm that all indentations made for hardness assessments were accurately positioned on the cross-sections of the samples. The results of these hardness measurements are presented in Fig. 7. The results indicate that the hardness of the Q235 steel is 152 $HV_{0.025}$. In contrast, the hardness values for the NiP-1, NiP-2, NiP-3, and NiP-4 samples are recorded as 341, 487, 629, and 839 $HV_{0.025}$, respectively. These findings suggest that electroless NiP alloy coatings of varying hardness levels were successfully fabricated on the surface of Q235 steel by adjusting the parameters of the electroless plating process.

Nano-indentation was used to determine the nano-hardness (H) and Young's modulus (E) of the NiP-1, NiP-2, NiP-3, and NiP-4 samples. The Young's modulus is a crucial parameter that measures the resistance of solid materials to deformation [34, 35]. In this context, the H/E and H^3/E^2 ratios, which represent resistance to elastic and plastic deformation, respectively, are often indicative of enhanced wear resistance [36]. As illustrated in Fig. 8, the surface nano-hardness of the NiP samples is consistent with the trends observed in the cross-sectional hardness tests. Specifically, the Young's moduli of the NiP-1, NiP-2, NiP-3, and NiP-4 samples are measured to be 165.63, 178.25, 185.30, and 216.22 GPa, respectively (Fig. 8(a)). This progression indicates an increase in stiffness corresponding with hardness. The H/E values for these samples are determined to be 0.0200, 0.0269, 0.0335, and 0.0380, respectively, while their H^3/E^2 values are 0.0013, 0.0035, 0.0069, and 0.0118, respectively, as shown in Fig. 8(b).

In the electroless plating process for NiP alloy coatings, variations in chemical composition and processing conditions play pivotal roles in modulating the nano-hardness and Young's modulus of the resulting coatings, as observed across the NiP-1 to NiP-4 samples. The increasing concentrations of key chemicals such as $NiSO_4$, NaH_2PO_2, $C_2H_3NaO_2$, and $C_3H_6O_3$ in NiP-3 and NiP-4, compared with those in NiP-1 and NiP-2, contribute to a

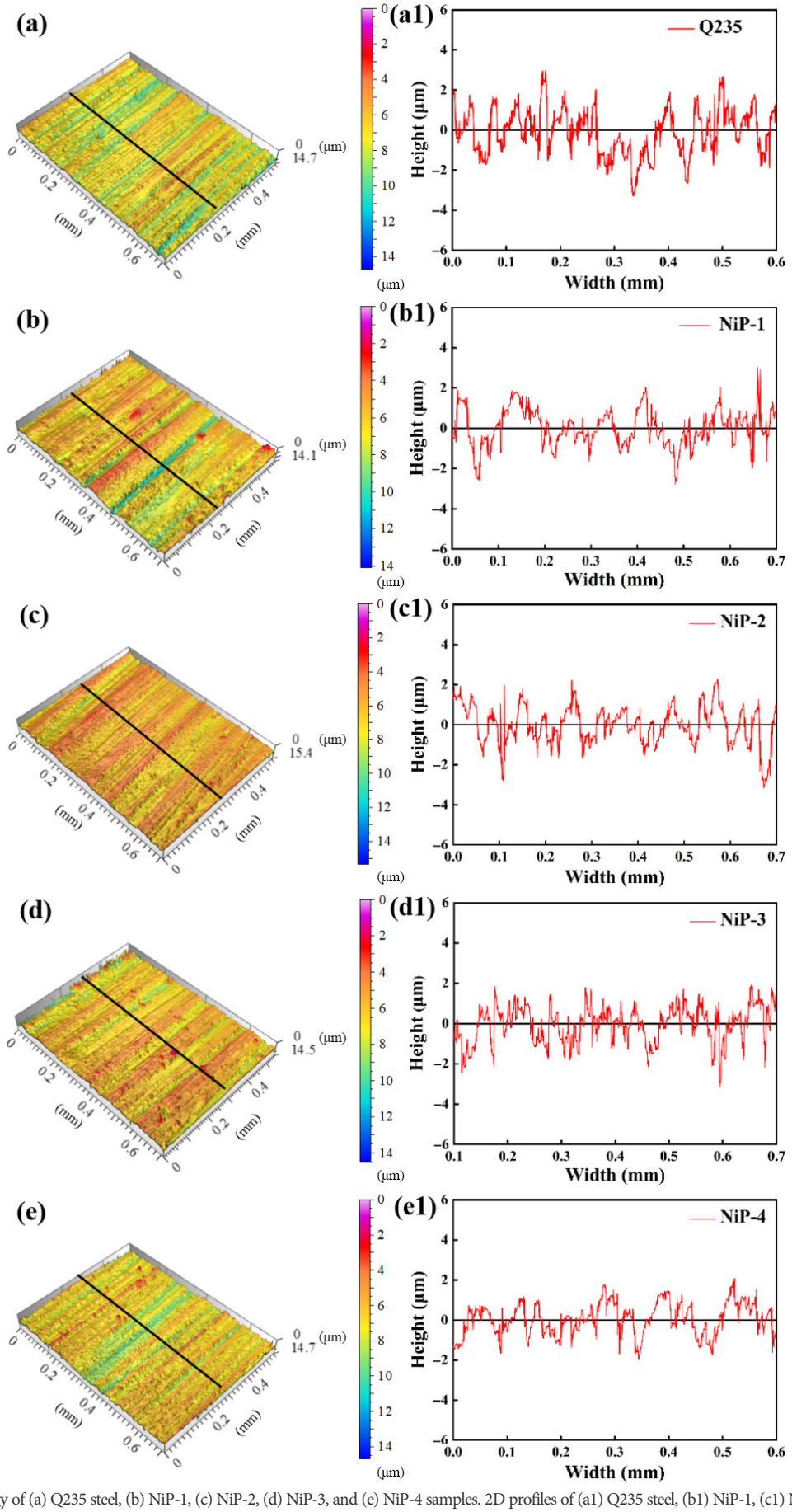

Fig. 4 3D morphology of (a) Q235 steel, (b) NiP-1, (c) NiP-2, (d) NiP-3, and (e) NiP-4 samples. 2D profiles of (a1) Q235 steel, (b1) NiP-1, (c1) NiP-2, (d1) NiP-3, and (e1) NiP-4 samples.

清華大学出版社 Tsinghua University Press | SciOpen

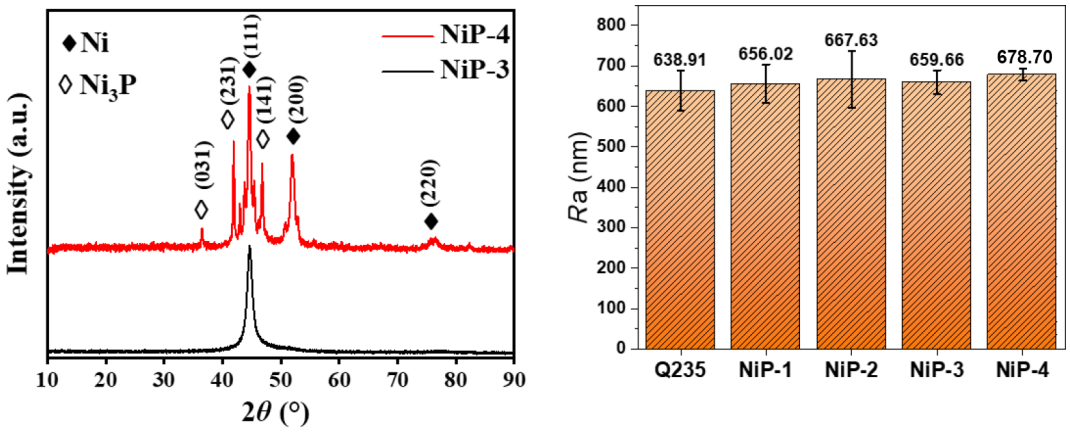

Fig. 5 Surface roughness of Q235 substrate and NiP-1-GO, NiP-2-GO, NiP-3-GO, and NiP-4-GO samples.

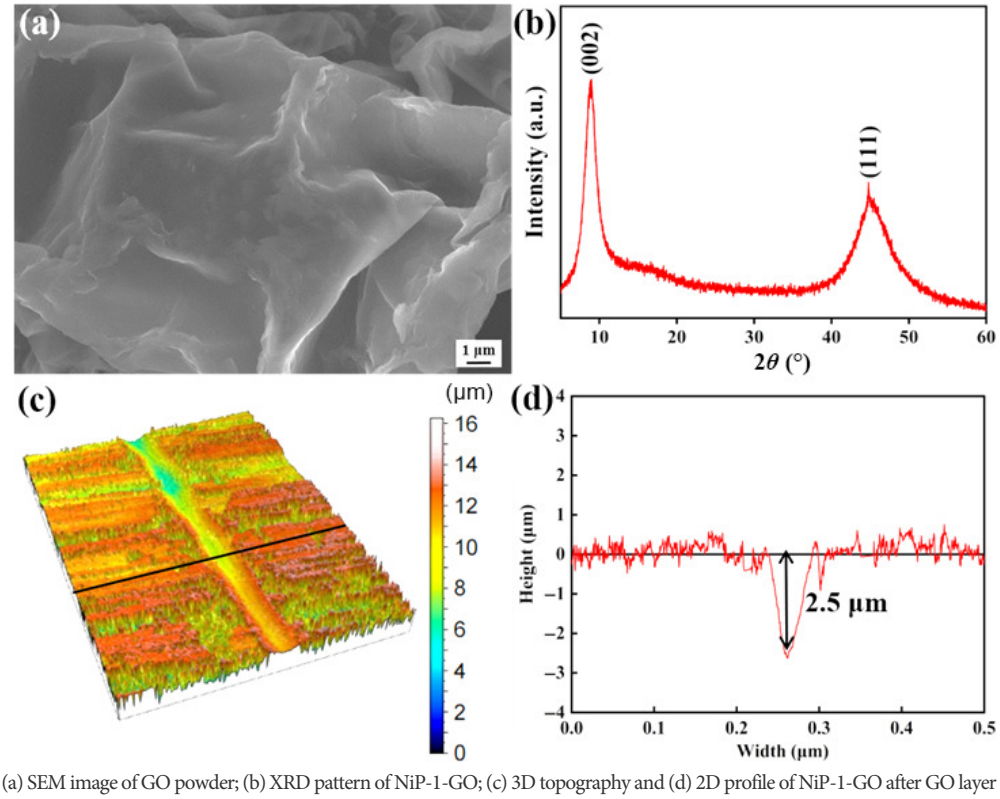

Fig. 6 (a) SEM image of GO powder; (b) XRD pattern of NiP-1-GO; (c) 3D topography and (d) 2D profile of NiP-1-GO after GO layer removal.

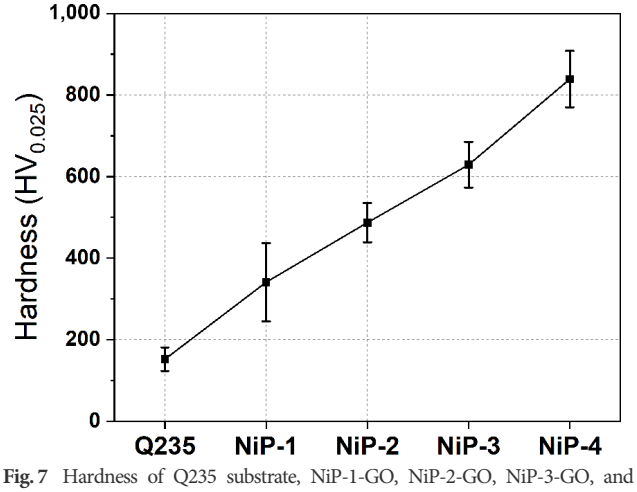

Fig. 7 Hardness of Q235 substrate, NiP-1-GO, NiP-2-GO, NiP-3-GO, and NiP-4-GO samples.

denser and more robust alloy microstructure. The introduction of specific additives, notably CH_4N_2S and KI, and the absence of $C_6H_5Na_3O_7{\cdot}2H_2O$ in NiP-3 and NiP-4 are likely to influence the deposition process, resulting in coatings with distinct microstructural characteristics. Furthermore, the exclusive heat treatment of NiP-4 at 400 °C for 60 min induces microstructural changes, such as grain growth or phase transformation, thereby increasing both the hardness and Young's modulus. These factors collectively account for the observed increment in the mechanical properties of the NiP coatings, indicating the importance of tailored chemical compositions and processing conditions in achieving the desired material characteristics.

3.4 Tribological performance of coatings

The friction coefficient curves for the NiP-1-GO, NiP-2-GO, NiP-3-GO, and NiP-4-GO samples are displayed in Fig. 9. In the case of NiP-1-GO, the friction coefficient initially decreased sharply from 0.17 to 0.12 within the first 4,000 cycles, followed by a stable stage before a significant rise at 21,800 cycles, indicating

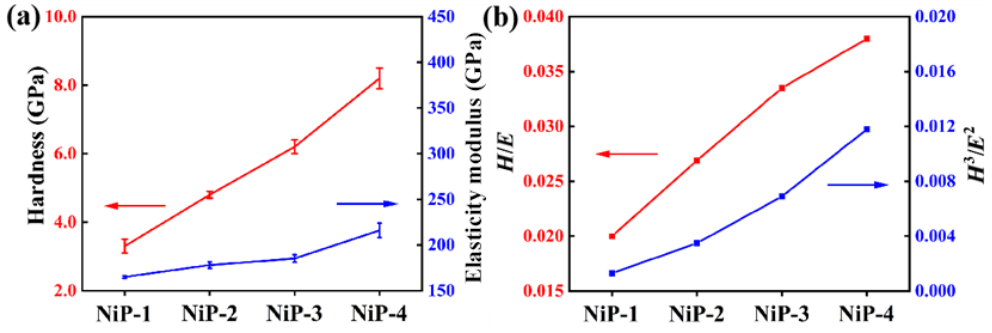

Fig. 8 (a) Nano-hardness and Young's modulus of NiP-1, NiP-2, NiP-3, and NiP-4 samples. (b) H/E and H^3/E^2 ratios of NiP-1, NiP-2, NiP-3, and NiP-4 samples.

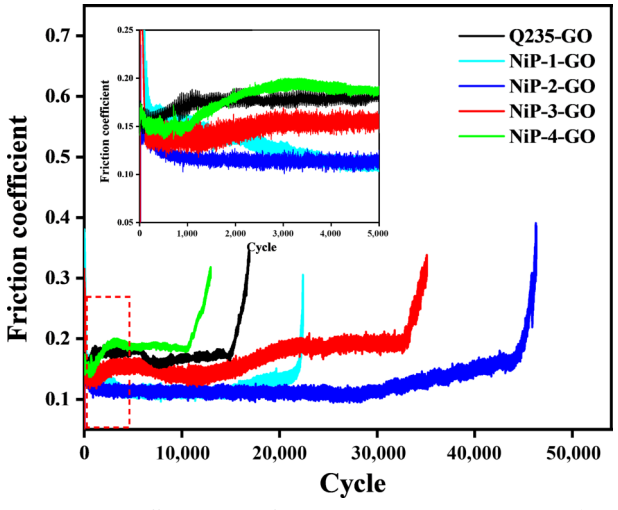

Fig. 9 Friction coefficient curves of NiP-1-GO, NiP-2-GO, NiP-3-GO, and NiP-4-GO samples.

the end of the lifetime of the coating. For NiP-2-GO, the friction coefficient quickly dropped from 0.15 to 0.11 within the initial 1,000 cycles and continued to decrease until it began to rise at approximately 30,000 cycles, leading to coating failure at 44,500 cycles. The friction coefficient of the NiP-3-GO sample initially increased to 0.15, then decreased to 0.14, and later increased to 0.19 at 20,100 cycles before the coating failure at 33,000 cycles. The friction coefficient of NiP-4-GO rose to 0.191 within 2,500 cycles, and after a period of stability, it rapidly increased, resulting in a coating lifetime of 10,000 cycles. The coating lifetimes of these samples follow a specific sequence, with NiP-2-GO, NiP-3-GO, NiP-1-GO, and NiP-4-GO ranking from the longest to the shortest. A lower friction coefficient during the stable stage is associated with an extended coating lifetime, indicating that the wear resistance of the samples is markedly influenced by the stability of the friction coefficient.

To elucidate the tribological mechanism underlying the relationships among the coating lifetime, friction coefficient, and substrate hardness, a detailed analysis of the wear tracks was performed. Raman spectroscopy was utilized to examine the NiP-1-GO, NiP-2-GO, and NiP-4-GO samples after 15,000 cycles, as shown in Fig. 10. The Raman spectra revealed two distinct band characteristics of GO: the D band at 1,360 cm^{-1}, indicative of structural defects such as sp^3 hybridized carbon atoms and edge defects, and the G band at 1,592 cm^{-1}, associated with the in-plane vibration of sp^2-bonded carbon atoms [37, 38]. Additionally, a band characteristic of Fe–O bond was observed at 613 cm^{-1}, assigned to the vibrational modes of E_g, reflecting the symmetric bending of oxygen atoms around iron in tetrahedral voids [39]. Figures 10(a) and 10(a1) depict the optical image and Raman spectra of NiP-1-GO, respectively. Notable wear at the asperity (A1) exposes a significant area of the substrate. The intensity of the GO band at A1 is decreased, whereas the Raman spectrum at the groove shows the typical D and G bands of GO, along with the Fe–O band, suggesting the accumulation of wear debris from the ball in the groove. For NiP-2-GO, as presented in Figs. 10(b) and 10(b1), GO is detected both at the asperity (A2) and within the groove (B2), indicating the timely release of GO in the groove during sliding, which mitigates extensive substrate exposure. Consequently, the NiP-2-GO sample exhibits a lower friction coefficient and the longest coating lifetime among the analyzed samples. In contrast, NiP-4-GO shows significant wear at the asperity (A4) as the substrate becomes exposed, and a considerable amount of lubricant accumulates in the groove (B4), as illustrated in Figs. 10(c) and 10(c1). While the G band is less prominent at A4, the Raman spectrum at the groove contains D and G bands corresponding to GO and Fe–O bond, indicating the storage of both the GO lubricant and the wear debris in the groove.

Further characterization was conducted on the wear tracks on the ball surfaces, and the results are shown in Figs. S1 and S2 in the Electronic Supplementary Material (ESM), which provide optical microscopy images and corresponding Raman spectra of wear tracks for NiP-1-GO, NiP-2-GO, and NiP-4-GO coatings after 30 and 50 min of sliding, respectively. After 30 min, the wear track diameters were 189, 236, and 262 μm for NiP-1-GO, NiP-2-GO, and NiP-4-GO, respectively, and the Raman spectra confirmed the formation of a GO tribofilm at both the track centers and edges. After 50 min, the diameter increased to 246, 244, and 280 μm. NiP-1-GO exhibited significant diameter growth, indicating tribofilm depletion and severe wear. NiP-2-GO demonstrated stable tribofilm retention, resulting in minimal diameter changes and effective lubrication. NiP-4-GO showed consistently larger diameters, suggesting reduced tribofilm stability and lubrication efficiency during prolonged sliding.

To ascertain the chemical state of the wear tracks, SEM and EDS analyses were performed on the wear tracks of NiP-1-GO and NiP-2-GO samples after 15,000 cycles of sliding. Figures S1 and S2 in the ESM depict the chemical element distributions in their wear tracks. The SEM images in Figs. S1(a) and S2(a) in the ESM reveal the wear tracks on NiP-1-GO and NiP-2-GO, respectively. Figures S1(b)–S1(f) and S2(b)–S2(f) in the ESM display the distributions of C, O, Ni, P, and Fe in both samples. According to the EDS elemental ratio analysis in Table 3, Ni and P elements are consistently distributed, reflecting the NiP alloy composition. Specifically, in NiP-1-GO, which experienced considerable wear, carbon is predominantly found in the grooves, with a reduced distribution of GO at the asperities, which is consistent with the Raman spectrum results (Fig. 10(a)). In contrast, NiP-2-GO exhibits a higher and more uniform surface

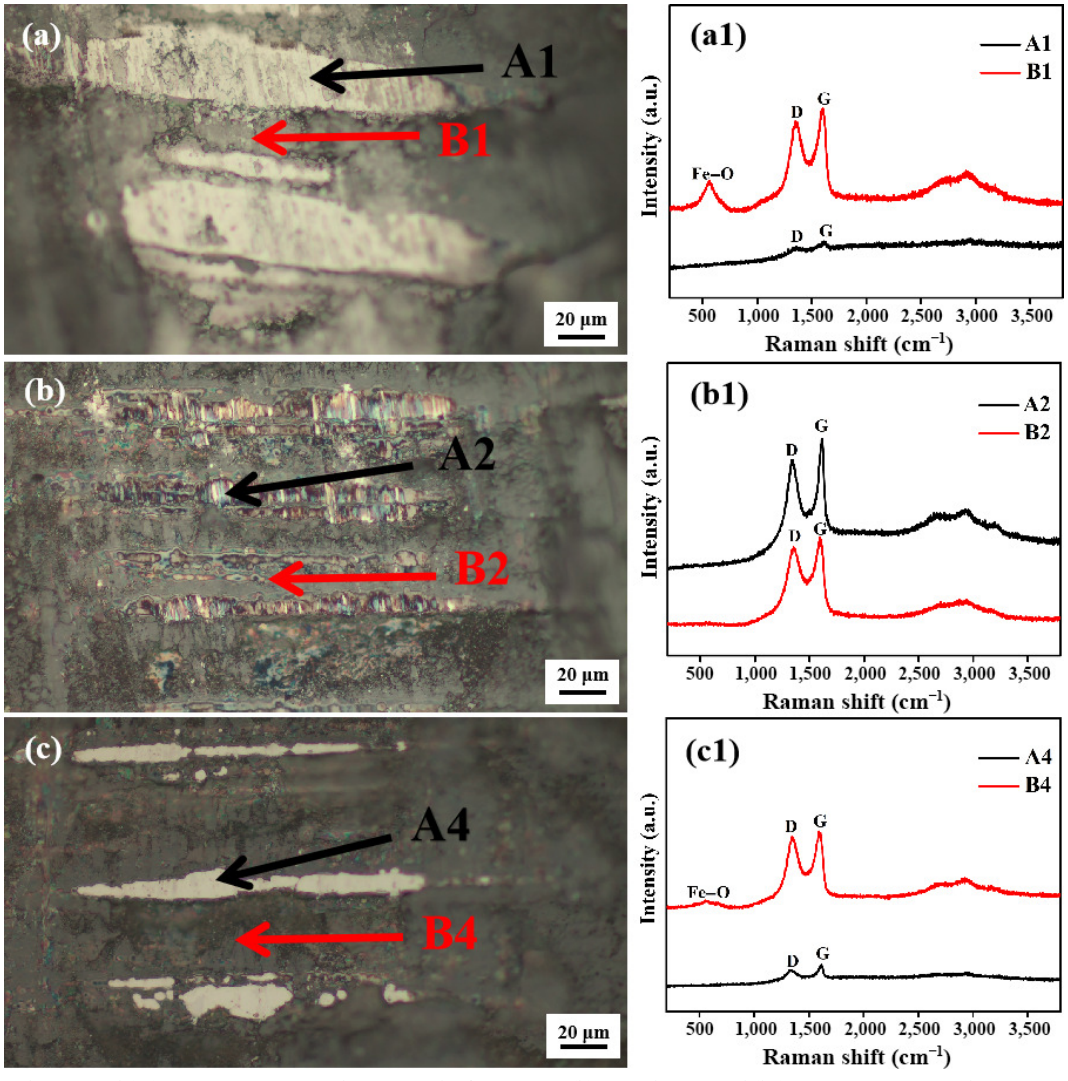

Fig. 10 (a) Optical image and (a1) Raman spectrum on the wear track of NiP-1-GO. (b) Optical image and (b1) Raman spectrum on the wear track of NiP-2-GO. (c) Optical image and (c1) Raman spectrum on the wear track of NiP-4-GO.

Table 3 Elemental composition of the wear tracks on NiP-1-GO and NiP-2-GO samples determined by EDS analysis (Unit: at%)

	C	O	Ni	P	Fe
NiP-1-GO	6.7	9.6	74.1	8.6	1.0
NiP-2-GO	10.4	15.3	64.9	8.4	1.0

concentration of carbon than NiP-1-GO. This uniform distribution of NiP-2-GO is instrumental in the sustained decrease in the friction coefficient over an extended period, resulting in a longer lifetime.

To explore the structural characteristics of the tribofilm, TEM measurements were carried out on the wear track. Figures 11 and 12 display the TEM images of the wear tracks on the NiP-2-GO and NiP-4-GO samples after 15,000 cycles of sliding. Figure 11(a) illustrates a variation in the tribofilm thickness, ranging from 163 nm at the valley to 140 nm at the peak of roughness. Figure 11(b) shows the tribofilm thickness at the highest peak, which changes from 52 to 81 nm. Figures 11(c) and 11(d) demonstrate the presence of both GO and NiO within the tribofilm, with the GO layer exhibiting no discernible lattice structure and the NiO layer having a lattice spacing of approximately 0.24 nm [40].

The TEM analysis of the NiP-4-GO sample, as presented in Fig. 13(a), reveals a prominent oxidation layer on the NiP layer, while a tribofilm is not distinctly observed. Figure 12(b) shows a discontinuous tribofilm within the wear groove. Additionally, Figs. 12(c) and 12(d) indicate that the NiO interlayer spacing in the oxidation layer is approximately 0.24 nm [41]. In contrast, the surface of the NiP-2-GO sample features a significant GO tribofilm, which plays a crucial role in enhancing its anti-wear lifetime compared with that of the NiP-4-GO sample.

TEM analysis revealed distinct structures in the wear tracks of the NiP-2-GO and NiP-4-GO samples. For NiP-2-GO, a significant and continuous GO tribofilm was observed, contributing substantially to its enhanced wear resistance and prolonged anti-wear lifetime. The moderate hardness of NiP-2-GO aids in the effective release of GO lubricant from valleys while providing adequate load-bearing capacity. The commendable tribological properties of this sample are attributed to the formation of a continuous tribofilm on the wear track, which minimizes direct contact and subsequent wear. Conversely, the NiP-4-GO sample displays a pronounced oxide layer on the topmost surface and lacks a continuous GO tribofilm, particularly

on the asperity peaks, leading to diminished wear resistance. Despite NiP-4 being the hardest substrate and ostensibly having superior load-bearing capacity, the failure to replenish its surface lubricant in a timely manner after consumption results in a discontinuous tribofilm. This discontinuity is a key factor in its reduced tribological effectiveness compared with that of NiP-2-GO.

3.5 Wear mechanism

In exploring the tribological behavior of coatings with varying hardnesses in the NiP layer, it becomes evident that the hardness level significantly influences their performance. Figure 13 schematically illustrates the mechanism of tribological behavior. In the initial stage, the GO layer is transferred to the counter surface, forming a transfer film, while a thin tribofilm simultaneously forms on the coating surface. This leads to reduced friction because sliding primarily occurs between these two films, which is attributed to the low shear strength of the GO layers [42]. The moderate hardness of 487 $HV_{0.025}$ in the NiP-2-GO sample ensures a continuous and uniform distribution of the GO tribofilm. This continuity is critical for the effective release of GO lubricant from the substrate grooves during sliding, which in turn contributes to consistent lubrication and enhanced load-bearing capacity. As a result, the NiP-2-GO sample, with its intermediate hardness, provides an optimal surface that not only resists excessive wear but also facilitates the effective release of the GO lubricant from surface grooves. This balance ensures consistent tribofilm formation during sliding, thereby maintaining low

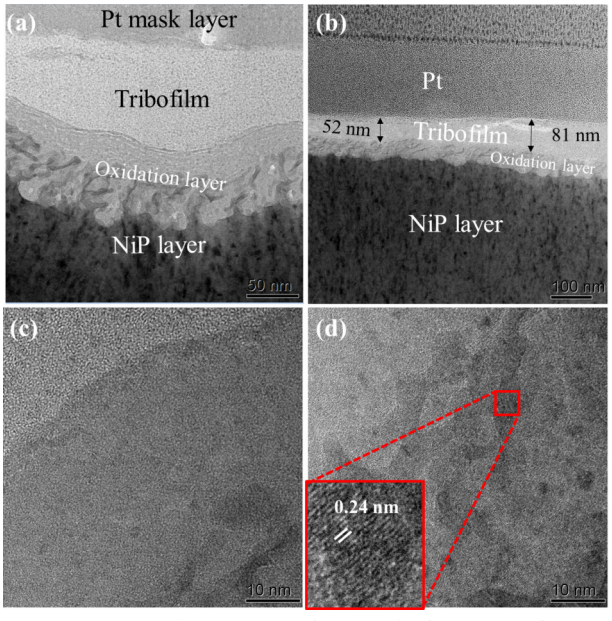

Fig. 11 Cross-sectional TEM images of wear track of NiP-2-GO after 15,000 cycles of sliding tests.

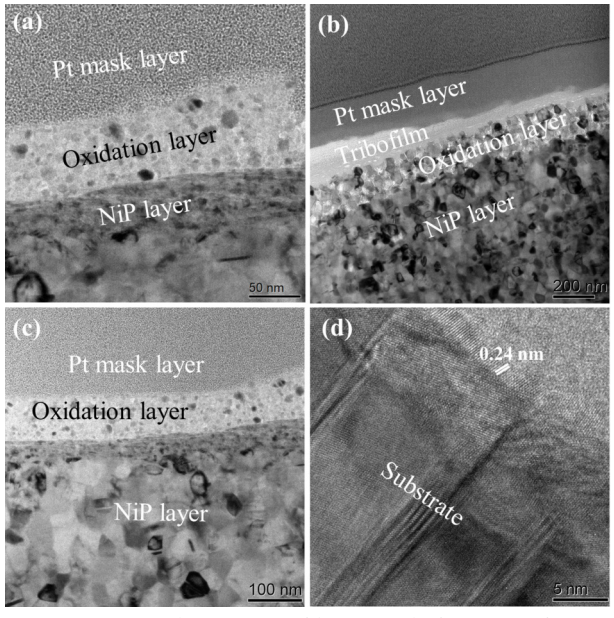

Fig. 12 Cross-sectional TEM images of the wear track of NiP-4-GO after 15,000 cycles of sliding tests.

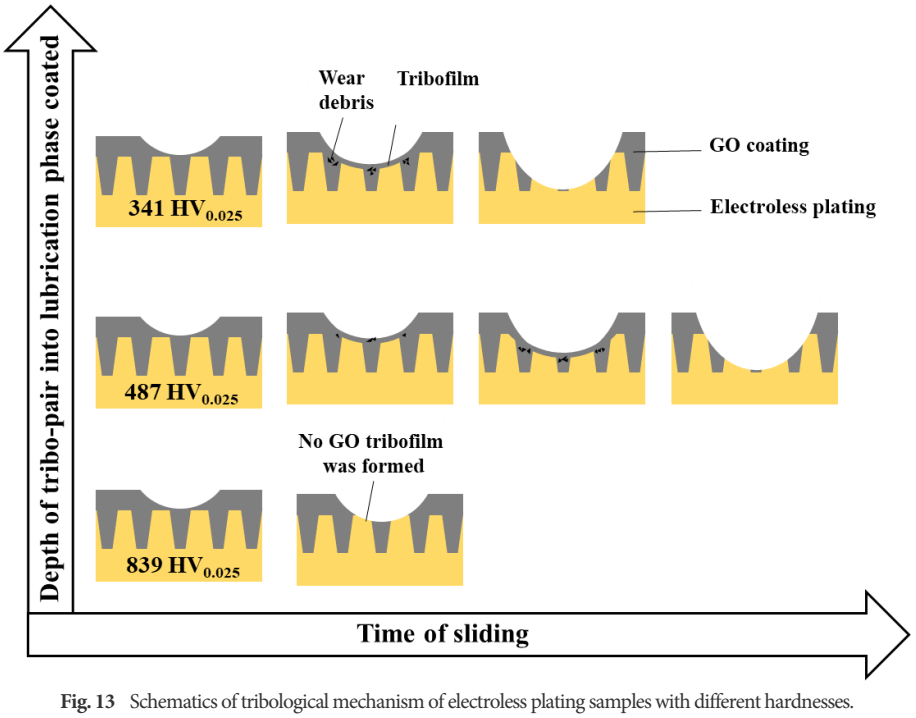

Fig. 13 Schematics of tribological mechanism of electroless plating samples with different hardnesses.

friction and reducing wear rates. Excessively hard substrates, such as NiP-4-GO, may prevent the effective release of GO, while softer substrates, such as NiP-1-GO, experience accelerated wear due to inadequate load support. The increased hardness of NiP-4-GO enhances the wear resistance of the substrate, making the asperity peaks difficult to wear during sliding and consequently hindering the release of GO. This leads to a discontinuous formation of the GO tribofilm, resulting in reduced tribological performance and a shorter anti-wear lifetime. For NiP-1-GO, with the lowest substrate hardness, the coating experiences pronounced substrate wear and substantial GO consumption, resulting in failure. These observations suggest that excessively high substrate hardness is detrimental to the effective functioning of solid lubricants. The wear mechanism of these coatings was clarified through the analysis of wear tracks and TEM images. For NiP-2-GO, the presence of a continuous and effective GO layer contributes to its superior wear resistance compared with that of NiP-4-GO, which lacks such a layer.

The ranking of the coating lifetimes (NiP-2-GO, NiP-3-GO, NiP-1-GO, and NiP-4-GO) is resulted from the complex tribological processes among coating removal, tribofilm formation, wear debris accumulation, and tribofilm transfer. Coating removal is influenced by substrate hardness and coating adhesion, where excessively hard substrates such as NiP-4-GO are prone to removal, and softer substrates such as NiP-1-GO experience faster wear under loading. Tribofilm formation plays a critical role, as the GO coating acts as a solid lubricant, forming a thin, stable tribofilm that reduces friction and wear. Coatings such as NiP-2-GO and NiP-3-GO, which have moderate substrate hardnesses, support consistent tribofilm formation and renewal, which contributes to their extended lifetimes. The tribofilm transfer, involving the movement of lubricating layers between contact surfaces, significantly impacts the performance of the coating. An optimal substrate hardness facilitates uniform tribofilm formation, maintaining lubrication and reducing wear rates. Coatings with either excessive or insufficient substrate hardness fail to sustain effective tribofilm formation, leading to shorter lifetimes. The findings of this study suggest that NiP-GO coatings could serve as potential materials for various industrial applications where enhanced surface properties are desirable. The improved hardness and wear resistance make these coatings promising candidates for use in the aerospace and automotive sectors, where components such as pistons, shafts, and gears require materials capable of reducing friction and extending service life.

4 Conclusions

This study comprehensively investigated the impact of substrate hardness on the tribological performance of solid lubricant coatings, with a focus specifically on NiP alloy layers of varying hardness applied to Q235 steel. The experimental results underscore the multifaceted influence of substrate properties on the effectiveness of GO as a solid lubricant. The varying hardness levels achieved through the electroless NiP plating process significantly affect the wear resistance and tribological behavior of the coated samples. The findings reveal that an optimal substrate hardness, such as that of NiP-2-GO sample, facilitates a continuous and uniform distribution of the GO tribofilm in the wear track. This uniformity is pivotal for ensuring consistent lubrication and improved load-bearing capacity, leading to a reduced friction coefficient and extended coating lifetime. This study demonstrates that moderate hardness levels are crucial for balancing the release of the solid lubricant and maintaining the integrity of the substrate under tribological stress. On the other hand, substrates with excessively high hardness, such as the NiP-4-GO sample, exhibit diminished tribological performance. Despite the superior wear resistance of the substrates, their inability to replenish the lubricant results in a discontinuous tribofilm, thereby compromising the lubricating efficiency and reducing the anti-wear lifetime. Conversely, substrates with relatively low hardness, such as NiP-1-GO, show rapid wear and depletion of the GO coating, leading to premature failure. This study underscores the critical importance of balancing substrate hardness with the characteristics of solid lubricants to optimize tribological performance. This study provides valuable insights into the design and application of surface treatments and coatings for industrial components, paving the way for more efficient, durable, and sustainable mechanical systems.

Acknowledgements

The authors are grateful for the funding from the Strategic Priority Research Program of the Chinese Academy of Sciences (No. XDB0470102), the Science and Technology Major Program of Gansu Province (No. 25ZDWA004), the National Natural Science Foundation of China (Nos. 52427807), the Key Research and Development Program in Shandong Province (No. SYS202203), the fund of the Chinese Academy of Sciences (No. PTYQ2024YZ0006), the Key Research Project of Shandong Provincial Natural Science Foundation (No. ZR2023ZD13), the Program for Taishan Scholars of Shandong Province, Lanzhou Institute of Chemical Physics (LICP) International Cooperative Scholarship, the Key Research Project of Shandong Provincial Natural Science Foundation (No. 2024KJHZ017), the Natural Science Foundation of Shandong Province (No. ZR2022QE162), the Provincial-Level Leading Talent Supporting Projects in Yantai City, the National Research Foundation of Korea (NRF) grant funded by the Korea government (MSIT) (RS-2025-00560422), the NRF grant funded by the Korea government (MOE) (4199990314094), and Yonsei University Research Fund (Post Doc. Researcher Supporting Program) of 2024 (2024-12-0194).

Declaration of competing interest

The authors have no competing interests to declare that are relevant to the content of this article. The authors Dae-Eun Kim and Weimin Liu are the Editorial Board Members of this journal.

Electronic Supplementary Material

Supplementary material is available in the online version of this article at https://doi.org/10.26599/FRICT.2025.9441085.

References

[1] Holmberg K, Kivikytö-Reponen P, Härkisaari P, Valtonen K, Erdemir A. Global energy consumption due to friction and wear in the mining industry. *Tribol Int* **115**: 116–139 (2017)

[2] Anand A, Irfan Ul Haq M, Vohra K, Raina A, Wani M F. Role of green tribology in sustainability of mechanical systems: A state of the art survey. *Mater Today—Proc* **4**(2): 3659–3665 (2017)

[3] Maboudian R, Ashurst W R, Carraro C. Tribological challenges in micromechanical systems. *Tribol Lett* **12**(2): 95–100 (2002)

[4] Donnet C, Erdemir A. Solid lubricant coatings: Recent developments and future trends. *Tribol Lett* **17**(3): 389–397 (2004)

[5] Franz R, Mitterer C. Vanadium containing self-adaptive low-friction hard coatings for high-temperature applications: A review. *Surf Coat Tech* **228**: 1–13 (2013)

[6] Aouadi S M, Gao H, Martini A, Scharf T W, Muratore C. Lubricious oxide coatings for extreme temperature applications: A review. *Surf Coat Tech* **257**: 266–277 (2014)

[7] Zhu S Y, Cheng J, Qiao Z H, Yang J. High temperature solid-lubricating materials: A review. *Tribol Int* **133**: 206–223 (2019)
[8] Wu S W, Tian S Y, Menezes P L, Xiong G P. Carbon solid lubricants: Role of different dimensions. *Int J Adv Manuf Tech* **107**(9): 3875–3895 (2020)
[9] Spear J C, Ewers B W, Batteas J D. 2D-nanomaterials for controlling friction and wear at interfaces. *Nano Today* **10**(3): 301–314 (2015)
[10] Kim S J, Cho M H, Cho K H, Jang H. Complementary effects of solid lubricants in the automotive brake lining. *Tribol Int* **40**(1): 15–20 (2007)
[11] Liu Y Z, Shin D G, Xu S S, Kim C L, Kim D E. Understanding of the lubrication mechanism of reduced graphene oxide coating via dual *in situ* monitoring of the chemical and topographic structural evolution. *Carbon* **173**: 941–952 (2021)
[12] Xu S S, Liu Y Z, Gao M Y, Kang K H, Kim C L, Kim D E. Selective release of less defective graphene during sliding of an incompletely reduced graphene oxide coating on steel. *Carbon* **134**: 411–422 (2018)
[13] Berman D, Erdemir A, Sumant A V. Reduced wear and friction enabled by graphene layers on sliding steel surfaces in dry nitrogen. *Carbon* **59**: 167–175 (2013)
[14] Reinert L, Schütz S, Suárez S, Mücklich F. Influence of surface roughness on the lubrication effect of carbon nanoparticle-coated steel surfaces. *Tribol Lett* **66**(1): 45 (2018)
[15] Dassenoy F. Nanoparticles as additives for the development of high performance and environmentally friendly engine lubricants. *Tribol Online* **14**(5): 237–253 (2019)
[16] Bhowmick S, Banerji A, Alpas A T. Role of humidity in reducing sliding friction of multilayered graphene. *Carbon* **87**: 374–384 (2015)
[17] Morstein C E, Dienwiebel M. Graphite lubrication mechanisms under high mechanical load. *Wear* **477**: 203794 (2021)
[18] Yao Q Z, Qi Y Z, Zhang J, Zhang S, Zhao P, Wang H T, Feng X Q, Li Q Y. Impacts of the substrate stiffness on the anti-wear performance of graphene. *AIP Adv* **9**(7): 075317 (2019)
[19] Gurrappa I. An oxidation model for predicting the life of titanium alloy components in gas turbine engines. *J Alloy Comp* **87**(1–2): 190–197 (2005)
[20] Carrera E, Rodríguez A, Talamantes J, Valtierra S, Colás R. Measurement of residual stresses in cast aluminum engine blocks. *J Mater Process Tech* **189**(1–3): 206–210 (2007)
[21] Liu Y Z, Han J H, Wang T, Hwang Y H, Xu S S, Liu W M, Kim D E. Tribochemical reaction and wear mechanism of MoDTC based friction modifier. *Tribol Int* **165**: 107302 (2022)
[22] Liu Y Z, Zhang K L, Han J H, Hwang Y H, Xu S S, Kim D E. One-step method to enhance biotribological properties and biocompatibility of DLC coating by ion beam irradiation. *Friction* **10**(7): 1114–1126 (2022)
[23] Shahriari A, Aghajani H. Electrophoretic deposition of 3YSZ coating on AZ91D alloy using Al and Ni–P interlayers. *J Mater Eng Perform* **25**(10): 4369–4382 (2016)
[24] Besra L, Liu M L. A review on fundamentals and applications of electrophoretic deposition (EPD). *Prog Mater Sci* **52**(1): 1–61 (2007)
[25] Ali Naziri Mehrabani S, Ahmadzadeh R, Abdian N, Taghizadeh Tabrizi A, Aghajani H. Synthesis of Ni–GO nanocomposite coatings: Corrosion evaluation. *Surf Interfaces* **20**: 100546 (2020)
[26] Lelevic A, Walsh F C. Electrodeposition of NiP alloy coatings: A review. *Surf Coat Tech* **369**: 198–220 (2019)
[27] Lucko G, Rojas E M. Research validation: Challenges and opportunities in the construction domain. *J Constr Eng M* **136**(1): 127–135 (2010)
[28] Chen W, Bao Z C, Zhou Z M. Selective hydrogenation of phenylacetylene over non-precious bimetallic Ni–Zn/SiO_2 and Ni–Co/SiO_2 catalysts prepared by glucose pyrolysis. *React Kinet Mech Cat* **135**(5): 2533–2550 (2022)
[29] Alvarez-Ramírez F, Toledo-Antonio J A, Angeles-Chavez C, Guerrero-Abreo J H, López-Salinas E. Complete structural characterization of $Ni_3Si_2O_5(OH)_4$ nanotubes: Theoretical and experimental comparison. *J Phys Chem C* **115**(23): 11442–11446 (2011)
[30] Samanta S, Mondal K, Dutta M, Singh S B. Electroless NiP coatings over API X70 steel: Effect of composition on the H-permeation and corrosion resistance. *Surf Coat Tech* **409**: 126928 (2021)
[31] Jin W, Pastor-Pérez L, Villora-Picó J J, Pastor-Blas M M, Odriozola J A, Sepúlveda-Escribano A, Reina T R. *In-situ* HDO of guaiacol over nitrogen-doped activated carbon supported nickel nanoparticles. *Appl Catal A—Gen* **620**: 118033 (2021)
[32] Zhang B A, Jiang Z Q, Shang X N, Li S S, Jiang Z J. Accelerated hydrogen evolution reaction in $Ni_3P/MoP_2/MoO_2$ tri-phase composites with rich crystalline interfaces and oxygen vacancies achieved by plasma assisted phosphorization. *J Mater Chem A* **9**(46): 25934–25943 (2021)
[33] Alzamly A, Bakiro M, Ahmed S H, Sallabi S M, Al Ajeil R A, Alawadhi S A, Selem H A, Al Meshayei S S M, Khaleel A, Al-Shamsi N, et al. Construction of BiOF/BiOI nanocomposites with tunable band gaps as efficient visible-light photocatalysts. *J Photoch Photobio A* **375**: 30–39 (2019)
[34] Carl P, Schillers H. Elasticity measurement of living cells with an atomic force microscope: Data acquisition and processing. *Pflug Arch Eur J Phy* **457**(2): 551–559 (2008)
[35] Badiche X, Forest S, Guibert T, Bienvenu Y, Bartout J D, Ienny P, Croset M, Bernet H. Mechanical properties and non-homogeneous deformation of open-cell nickel foams: Application of the mechanics of cellular solids and of porous materials. *Mater Sci Eng A* **289**(1–2): 276–288 (2000)
[36] Musil J, Kunc F, Zeman H, Poláková H. Relationships between hardness, Young's modulus and elastic recovery in hard nanocomposite coatings. *Surf Coat Tech* **154**(2–3): 304–313 (2002)
[37] Claramunt S, Varea A, López-Díaz D, Velázquez M M, Cornet A, Cirera A. The importance of interbands on the interpretation of the Raman spectrum of graphene oxide. *J Phys Chem C* **119**(18): 10123–10129 (2015)
[38] Kudin K N, Ozbas B, Schniepp H C, Prud'homme R K, Aksay I A, Car R. Raman spectra of graphite oxide and functionalized graphene sheets. *Nano Lett* **8**(1): 36–41 (2008)
[39] Rajpure K Y. Exploring structural and magnetic properties of nanocrystalline iron oxide synthesized by autocombustion method. *Superlattice Microst* **77**: 181–195 (2015)
[40] Zhao L, Zhang Y, Zhao Z L, Zhang Q H, Huang L B, Gu L, Lu G, Hu J S, Wan L J. Steering elementary steps towards efficient alkaline hydrogen evolution via size-dependent Ni/NiO nanoscale heterosurfaces. *Natl Sci Rev* **7**(1): 27–36 (2020)
[41] Wang L, Huang Y, Sun X, Huang H J, Liu P B, Zong M, Wang Y. Synthesis and microwave absorption enhancement of graphene@Fe_3O_4@SiO_2@NiO nanosheet hierarchical structures. *Nanoscale* **6**(6): 3157–3164 (2014)
[42] Wu P, Li X M, Zhang C H, Chen X C, Lin S Y, Sun H Y, Lin C T, Zhu H W, Luo J B. Self-assembled graphene film as low friction solid lubricant in macroscale contact. *ACS Appl Mater Inter* **9**(25): 21554–21562 (2017)

Yuzhen Liu is currently a postdoctoral fellow at the Tribology Research Laboratory in the Department of Mechanical Engineering at Yonsei University Graduate School. Under the guidance of Professor Dae-Eun Kim, Yuzhen focused on *in situ* Raman spectroscopy analysis and studying the influence of microstructure on tribological behavior. Before joining Yonsei University, Yuzhen worked at the Lanzhou Institute of Chemical Physics, Chinese Academy of Sciences (CAS).

Hui Chen works as an associate professor at China University of Mining and Technology (CUMT). He received his bachelor and M.S. degrees in material science and engineering in 2006 from CUMT. After that, he obtained his Ph.D. degree in mineral materials engineering at the same school. His research interests include wear-resistant steel, fuel cells, and nanocomposite materials.

Shusheng Xu is currently a professor at the State Key Laboratory of Solid Lubrication (LSL), Chinese Academy of Sciences. Before joining LSL, he worked as a research fellow at the University of Leeds from February 2018 to January 2020 and as a postdoctoral research associate at Yonsei University from August 2016 to January 2018. The main research interest of his group is the design and preparation of functional coatings for surface engineering, including vapor deposition of coating materials for addressing the growth mechanism and coating structure design, especially transition metal dichalcogenides, ceramics and diamond-like carbon (DLC), and their applications in extreme space environments. Currently, he has published more than 50 papers and has 10 invention patents.

Dae-Eun Kim, is currently a full professor at the School of Mechanical Engineering, Yonsei University. Professor Kim received his Ph.D. degree in mechanical engineering from the Massachusetts Institute of Technology (MIT). Professor Kim served as the president of both the Korean Society for Precision Engineering and the Korean Tribology Society. He also served as the editor-in-chief of *International Journal of Precision Engineering and Manufacturing*, senior editor of *Journal of Mechanical Science and Technology*, and associate editor of *the American Society of Mechanical Engineers Journal of Tribology*. He currently serves on the editorial board of several tribology journals, including *Tribology Letters* and *Friction*. Professor Kim has received many awards from various professional societies and institutions, including the Ministerial Commendation from the Korea Ministry of Trade, Industry and Energy and the Science and Technology Pojang National Award from the Korean President. Professor Kim is a fellow of the International Academy for Production Engineering (CIRP) and a fellow of the Korean Academy of Science and Technology. His research interests are tribology, coating, and surface modification.

Weimin Liu received his Ph.D. degree in lubricating materials and tribology from Lanzhou Institute of Chemical Physics (LICP), CAS, in 1990. After that, he joined the State Key Laboratory of Solid Lubrication (LSL) in LICP. From June 1993 to June 1994, he worked as a visiting scholar at Pennsylvania State University. In 2013, he was elected the member of the CAS. Currently, he is a professor of LICP and head of the LSL. Up to now, he has published more than 500 papers with citation over 38,000. He holds 80 Chinese patents and 1 U.S. patent, and has won 3 National Awards for Technological Invention (second class) and 2 National Awards for Natural Sciences (second class). Currently, his research interests mainly focus on space and aviation lubrication, high performance lubricating materials, and tribochemistry.